Explicit solutions of the Kapchinskij-Vladimirskij equations for quadrupoles with unequal drift lengths, arbitrary eld strength, and undepressed tune

O. A. Anderson
LBNL, Berkeley, CA 94720, USA

L. L. LoDestro
LLNL, Livermore, CA 94551, USA

Explicit solutions of the Kapchinskij-Vladimirskij equations for quadrupoles with unequal drift lengths, arbitrary field strength, and undepressed tune

O. A. Anderson

LBNL, Berkeley, CA 94720, USA

L. L. LoDestro

LLNL, Livermore, CA 94551, USA

(Dated: September 10, 2012)

In 1958, Courant and Snyder analyzed alternating-gradient beam transport using a paraxial model without focusing gaps or space charge. Recently we revisited their work and found the exact solution for matched-beam envelopes in a linear quadrupole lattice [O.A. Anderson and L.L. LoDestro, Phys. Rev. ST Accel. Beams, 2009]. We extend that work here to include the effect of drift spaces, not necessarily of equal length. We calculate the exact envelopes and show results for a wide range of field strengths, occupancies, and drift-length ratios. We obtain an exact equation for the peak envelope excursion, a critical parameter in machine design. We discuss how this result can be used to find a favorable operating point (in terms of focus strength or phase advance σ_0) for an arbitrary lattice configuration. The smallest excursions always occur in the first stable band ($0° < \sigma_0 < 180°$) in a region near its midpoint; and their amplitude is remarkably insensitive to the drift-space geometry. The exact solutions for the second stable band ($180° < \sigma_0 < 360°$) exhibit the extreme beam-compression effect discussed in the above reference. Practical difficulties discussed there for possible applications are seen to be exacerbated by the inclusion of drift spaces. Finally, we show how to scale our exact results to approximate the effect of strong space charge.

I. INTRODUCTION

In their classic paper, Courant and Snyder [1] studied paraxial beam-envelope dynamics in a circular machine with negligible space charge, using the piecewise-constant focus-defocus (FD) model. They obtained an approximate solution for the envelope, using an expansion in focusing strength. For a straight machine, the same case was recently analyzed and an exact solution in explicit form was obtained [2], [3]. In the present paper we extend that work to include focusing gaps, which are allowed to have unequal lengths (syncopation). Particular cases with unequal gaps have long been studied via computer simulations; an especially thorough study of the KV equations [4] (including space charge) was published by Lund and Bukh [5].

Our three main motivations for presenting the explicit analytic envelope function for this case are: (1) ease of performing parametric studies such as those shown in Fig. 2, Fig. 5, and App. D, using simple spreadsheets; (2) ability to analyze solution properties such as extrema and limits (Sec. VIII); and (3) facilitating the study of envelope functions in the higher stable bands (Figs. 4 and 6), where approximation methods fail and simulations become difficult. In particular, we are interested in the effect of drift spaces and asymmetry on the pronounced second-band beam compression effect found earlier for the FD model.

Our piece-wise constant focusing model, while not realistic, can represent physical models fairly well if η is appropriately chosen [5], [6]. In any case, our studies here should give good insight into the trends in physical models.

In this paper, instead of using the direct approach of Ref. [3], we obtain the exact envelope functions and phase advances by using the linear single-particle equation and the phase-amplitude method (Apps. A and B). A condensed version of this work was presented in Ref. [7].

Our exact results do not include space charge, but its effect can be approximated by scaling (Sec. VII D). The scaled results could provide good starting seeds for difficult simulations with strong asymmetry and space charge.

To indicate briefly that our doublet model includes piecewise-constant focusing and unequal drift spaces, we introduce the abbreviation *FoDO*.

II. FoDO FOCUSING MODEL

We assume a transverse linear focusing function $\kappa(z)$ that is periodic over a lattice with period $2L$, so that $\kappa(z + 2L) = \kappa(z)$. We take $\kappa(z)$ to be piecewise constant with value $+\kappa_{max}$ in the focus and $-\kappa_{max}$ in the defocus sections. These sections have length ηL, where η is the occupancy factor. The intervening drift sections have lengths d_1 and d_2, where $d_2 \geq d_1$ is assumed. For convenience throughout, we define

$$k \equiv \sqrt{\kappa_{max}}. \tag{1}$$

Our model is then described for the x-z plane by Eqs. (2) and Fig. 1:

$$\kappa(z) \equiv \begin{cases} +k^2, & 0 < z < \eta L; \\ 0, & \eta L < z < \eta L + d_1; \\ -k^2, & \eta L + d_1 < z < 2\eta L + d_1; \\ 0, & 2L - d_2 < z < 2L. \end{cases} \tag{2}$$
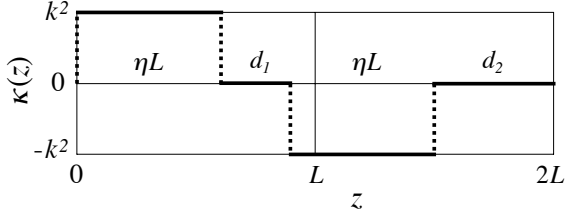
FIG. 1. Focusing model for one cell of a periodic FoDO lattice, which begins at $z = 0$. The section lengths are ηL for the quadrupoles and d_1 and d_2 for the drifts. The x-z plane, shown here, starts with $\kappa > 0$ (focus). For the y-z plane (not shown), κ is replaced by -κ.

Drift centers z_c:

Since the FoDO lattice cell has equal focus and defocus lengths, the fields have antisymmetry about each drift center z_c. These centers have spacing L. For a matched beam, this antisymmetry yields a relationship between the envelopes $a(z)$ and $b(z)$ in the x-z and y-z planes, respectively. Using arguments similar to those in Ref. [6], we find that

$$b(z) = a(2z_c - z), \tag{3}$$

where z_c is any drift center, so that we only need to solve one differential equation [for $a(z)$] in what follows.

Symmetries and initial conditions:

Section VII, along with the appendices, derives the formula for the exact envelope function. There are three types of cases for our model: (i) no drift spaces, i.e., $\eta = 1$; (ii) equal drift spaces, i.e., $\mu = 0$ [see Eq. (4)]; and (iii) unequal drift spaces. In the first two cases, in addition to the above antisymmetry, there is symmetry about the quadrupole midpoints. It follows that, for these two cases, $a(z)$ and $b(z)$ are even about those midpoints. All three cases are illustrated in Figs. 3 and 4.

From Eq. (3), the initial conditions for a matched beam, starting at a drift center, are $a(z_c) = b(z_c)$ and $a'(z_c) = -b'(z_c)$.

III. DEFINITIONS

A. Drift asymmetry parameter μ

We define the drift asymmetry parameter μ (where $0 \leq \mu \leq 1$):

$$\mu \equiv \frac{d_2 - d_1}{2d}, \tag{4}$$

where d is the average drift length:

$$d \equiv \frac{d_2 + d_1}{2} = (1 - \eta)L. \tag{5}$$

Then

$$d_1 = d(1 - \mu), \qquad d_2 = d(1 + \mu). \tag{6}$$

The normalized drift lengths, for use in Sec. V, are

$$\nu_1 \equiv kd_1 = \nu(1 - \mu), \tag{7}$$

$$\nu_2 \equiv kd_2 = \nu(1 + \mu), \tag{8}$$

$$\nu \equiv kd = k(1 - \eta)L = \frac{1 - \eta}{\eta}\,\theta, \tag{9}$$

where θ is defined by Eq. (10) below.

B. The FoDO focus parameter θ

The FoDO focus parameter θ, used throughout this paper, is defined by

$$\theta \equiv \eta kL. \tag{10}$$

We introduce the following quantities that depend on θ:

$$sn \equiv \sin\theta, \qquad cs \equiv \cos\theta,$$

$$sh \equiv \sinh\theta, \qquad ch \equiv \cosh\theta. \tag{11}$$

Note: Ref. [3], which considered $\eta = 1$ only, used the symbol θ to stand for kL. Our new definition is an extension of that usage. All the results in this paper reduce to those in [3] in the FD full-occupancy limit. [See note after Eq. (32).]

IV. SOLUTION OF THE ENVELOPE EQUATION

The discussion in this section applies to the general case of an arbitrary periodic focus-function $f(z)$. For a beam with the KV distribution, emittance $\in$, and space-charge term Sp, the x-z plane envelope function $a(z)$ is determined by [4]:

$$a''(z) + f(z)\,a - \frac{\in^2}{a^3} + Sp = 0 \tag{12}$$

along with initial or periodic conditions for a and b. In this paper we assume $\in_x = \in_y = \in$. We neglect the space-charge term Sp — except for the discussion in Sec. VII D. (We also note that in the absence of space charge, the KV distribution can be replaced by a class of physically realistic distributions.)

For a matched beam without space charge, it is unnecessary to solve the nonlinear Eq. (12) directly, as we did in Ref. [3]. Instead, one can begin with the linear single-particle equation

$$x''(z) + f(z)\,x(z) = 0 \tag{13}$$

and use the phase-amplitude method [1] to find the envelopes. We review this in Apps. A and B.

The appendices give an elementary derivation (not requiring Twiss parameters or the Courant-Snyder invariant) of the well-known envelope solution, Eq. (B4). We repeat that result here for convenience:

$$\frac{1}{\in}a^2(z) = \frac{M_{12}(z)}{P\sqrt{1 - (\frac{1}{2}\text{Tr}\,\mathbf{M})^2}}, \qquad (14)$$

where $\mathbf{M}$ is the advance matrix for one cell of an arbitrary periodic lattice and P is the sign function, defined in Eq. (B6). For any focus parameter θ, P provides the correct sign for the radical.

For the particular cell model in which the focus function $f(z)$ consists of segments having constant focus strength, the matrix $\mathbf{M}$ is the product of the transfer matrices for the individual segments. Figure 1 shows the FoDO model. The four segments—taken in the order shown in the figure—have transfer matrices given by [1], [8]:

$$\mathbf{M}_F = \begin{pmatrix} cs & \frac{1}{k}sn \\ -k\,sn & cs \end{pmatrix}, \qquad (15)$$

$$\mathbf{M}_{O_1} = \begin{pmatrix} 1 & d_1 \\ 0 & 1 \end{pmatrix}, \qquad (16)$$

$$\mathbf{M}_D = \begin{pmatrix} ch & \frac{1}{k}sh \\ k\,sh & ch \end{pmatrix}, \qquad (17)$$

$$\mathbf{M}_{O_2} = \begin{pmatrix} 1 & d_2 \\ 0 & 1 \end{pmatrix}. \qquad (18)$$

The matrix for the entire cell (Fig. 1), starting at $z = 0$, is

$$\mathbf{M}(0) = \mathbf{M}(2L) = \mathbf{M}_{O_2}\mathbf{M}_D\,\mathbf{M}_{O_1}\mathbf{M}_F. \qquad (19)$$

The ranges of z for the four individual segments are indicated in Fig. 1. If z does not fall on a segment boundary, then the segment splits into two subranges—for example, z and $(\eta L - z)$ if z is in the first segment. There are then five component matrices, as in Sec. VII A.

V. PHASE ADVANCE AND STABILITY

Reference [1] shows that a single-particle orbit is stable if

$$|\text{Tr}\,\mathbf{M}| < 2 \qquad (20)$$

and that $\text{Tr}\,\mathbf{M}$ is independent of z. (Cf. App. A, Eq. A11.) We calculate the trace at $z = 0$, using $\mathbf{M}(0)$ from Eq. (19). First, we introduce a matrix that will be used again in Sec. VII A:

$$\mathbf{M}_{\text{III}} \equiv \mathbf{M}_{O_2}\mathbf{M}_D\,\mathbf{M}_{O_1} = \begin{pmatrix} A_1 & \frac{2B+sh}{k} \\ k\,sh & A_2 \end{pmatrix}, \qquad (21)$$

with A_1 and A_2 defined by

$$A_1 \equiv ch + \nu_2\,sh, \qquad A_2 \equiv ch + \nu_1\,sh, \qquad (22)$$

and B by

$$B \equiv \nu\,ch + \frac{1 - \mu^2}{2}\nu^2 sh. \qquad (23)$$

Then

$$\mathbf{M}(0) = \begin{pmatrix} A_1 & \frac{2B + sh}{k} \\ k\,sh & A_2 \end{pmatrix} \begin{pmatrix} cs & \frac{1}{k}sn \\ -k\,sn & cs \end{pmatrix}.$$

Phase advance σ_0 for a whole period

It is unnecessary to write all the components of the full matrix in order to find the phase advance. Only M_{11} and M_{22} are needed, according to Eq. (B2). Thus,

$$\cos\sigma_0 = \frac{\text{Tr}\,\mathbf{M}}{2} = (ch + \nu\,sh)cs - B\,sn, \qquad (24)$$

which agrees with the result given by Lund and Bukh [5].

Stability

The envelope solution will be stable for all values of θ for which the right-hand side of Eq. (24) lies within the range $[-1, 1]$. Such regions of θ are referred to as stable bands or passbands. Reference [3] shows how these bands are related to the branches of $\cos\sigma_0$. Using appropriate branches of Eq. (24), the phase advance is plotted as a function of kL/π in Fig. 2 for various values of occupancy η and drift asymmetry μ. Drift spaces provide no focusing, so reducing η requires increasing kL to achieve a given phase advance. Figure 2 shows this and shows the effect to be stronger in the second passband. Another effect of reducing η is seen: In the first panel of Fig. 2, the fractional width $(\Delta kL/kL)$ of the second passband at full occupancy is 0.763%. This fraction is reduced significantly for half occupancy, becoming 0.263% and 0.279% in the second and third panels, respectively. Related results are discussed in Sec. VII C.

VI. PASSBAND MIDPOINTS

We define the midpoint of any passband as the point where $\text{Tr}\,\mathbf{M} = 0$, i.e., where

$$\sigma_0 = \sigma_{0n} = 90° + (n - 1)180° \qquad (25)$$

with n the passband number.

We define the midpoint focus parameter θ_n of the nth passband as the value of θ that satisfies

$$\text{Tr}\,\mathbf{M}(\theta_n) = 0. \qquad (26)$$

An examination of Eq. (24) provides insight into the effects of varying η and μ. In the special case $\eta = 1$, Eq. (24) gives $\cos\sigma_0 = ch\,cs$; thus $\theta_n = \sigma_{0n} = (n-$

$\frac{1}{2})\pi$. Both θ and σ_0 advance by π between midpoints of successive passbands—see the top row of Fig. 2.

For general η, Eq. (24) gives

$$\tan\theta_n = (ch + \nu\, sh)/B \Big|^{\theta=\theta_n}, \qquad (27)$$

where the right-hand side is a positive single-valued function of θ_n. Thus, for general η and μ, there continues to be one passband for each interval of π in θ.

Equation (27) is useful for finding the location of the narrow second passband in θ space, given η and μ (see App. F). Note that although $\theta \approx \theta_n$ in the higher passbands, σ_0 still varies over the range of $180°$ and the solution still changes drastically near the band edges.
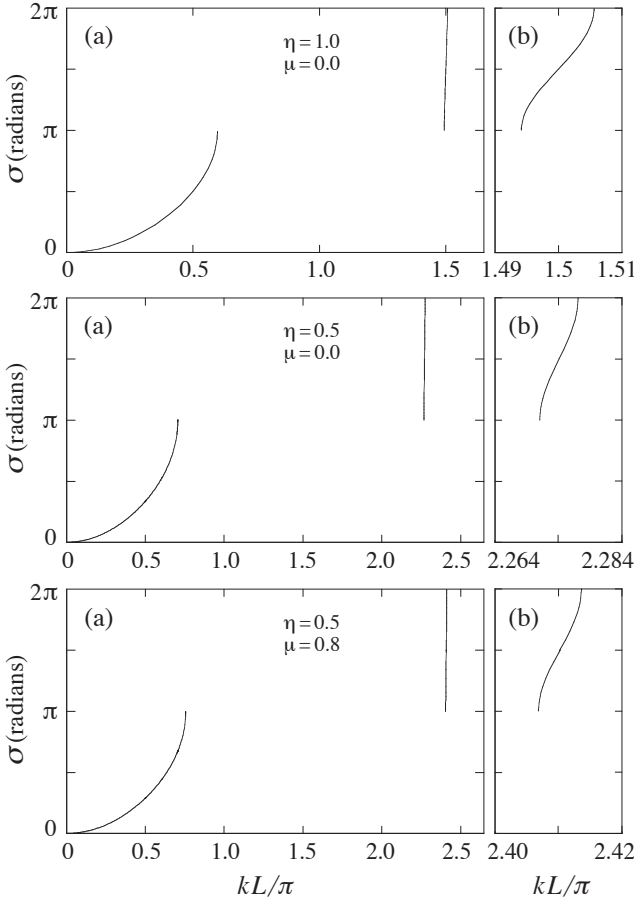

FIG. 2. (a) Phase advances calculated from Eq. (24) for the first two stable bands. (b) The second band repeated, with the kL axis magnified. Occupancies are $\eta = 1.0$ for the top panel and $\eta = 0.5$ for the others. The bottom panel has drift-space asymmetry $\mu = 0.8$. Note that introducing drift spaces narrows the second passband (see text).

VII. EXPLICIT ENVELOPE FOR FoDO STABLE BANDS

A. Focus segment

Now we are ready to use Eq. (14) to find the envelope function. We begin with the first (focus) segment of the lattice. For an arbitrary point z in this segment, the full-period transfer matrix is obtained from $\mathbf{M}_{\mathrm{III}}$ after pre- and post-multiplying by the two subunits of $\mathbf{M}_F$ mentioned at the end of Sec. IV. Using Eq. (21), we have

$$\mathbf{M}^F(z) = \begin{pmatrix} \cos kz & \frac{1}{k}\sin kz \\ -k\sin kz & \cos kz \end{pmatrix} \begin{pmatrix} A_1 & \frac{2B + sh}{k} \\ k\, sh & A_2 \end{pmatrix} \times$$
$$\begin{pmatrix} \cos k(\eta L - z) & \frac{1}{k}\sin k(\eta L - z) \\ -k\sin k(\eta L - z) & \cos k(\eta L - z) \end{pmatrix}. \quad (28)$$

The superscript F signifies that z is restricted here to the focusing segment of the quadrupole cell. The matrix multiplications are a bit tedious, but to find $a(z)$ we only need the element M^F_{12}. It is:

$$2k\mathrm{M}^F_{12} = (A_1 + A_2)sn + (A_1 - A_2)\sin[k(\eta L - 2z)]$$
$$+ 2B\, cs + (2B + 2\, sh)\cos[k(\eta L - 2z)]. \quad (29)$$

Finally, we define

$$F^F(z) \equiv k\mathrm{M}^F_{12} \qquad (30)$$

and use Eqs. (10), (14) and (22) to get the exact result for the focus-segment envelope. It is

$$a^2(z) = \in\eta L\, \frac{F^F(z)}{\mathrm{P}\,\theta\,\sqrt{1 - (\frac{1}{2}\mathrm{Tr}\,\mathbf{M})^2}} \qquad (31)$$

with $\mathrm{Tr}\,\mathbf{M}$ from Eq. (24) and

$$F^F(z;\theta,\mu,\nu) = (ch + \nu\, sh)sn + \mu\nu\, sh\sin[\theta(1 - 2z/\eta L)]$$
$$+ B\, cs + (B + sh)\cos[\theta(1 - 2z/\eta L)]. \quad (32)$$

We have introduced the dimensionless quantity F^F—rather than using M^F_{12} as in Eq. (14)—in order to clarify the dependence on the focus parameter θ.

When $\nu = 0$, then $\eta = 1$ (i.e., there is full occupancy) and $B = 0$. In this case Eq. (31) reduces to the previous result for FD focusing [3], which was derived by a different method. (See also the note at the end of Sec. III.)

B. Drift and defocus segments

The beam envelopes for the three other segments in the FoDO lattice cell are given in App. C. These exact results for $a(z)$ [Eqs. (C8), (C9), and (C10)] were used,

along with Eq. (31), for the figures in this section. The transverse envelope $b(z)$ was easily obtained from $a(z)$ using Eq. (3).

Figures 3 and 4 plot the normalized envelope functions

$$a_{\text{norm}} \equiv a(z)/\sqrt{\in L} \quad \text{and} \quad b_{\text{norm}} \equiv b(z)/\sqrt{\in L} \qquad (33)$$

for several combinations of occupancy and drift asymmetry. In these figures, $z = 0$ at the beginning of the focus section as in Fig. 1, but the plots are shifted in order to display the matched-beam symmetry described in Sec. II. The plots start at the center of the second drift space.

C. Variability of peak envelope

First passband:

The peak envelope amplitudes (1.740, 1.776, 1.761, and 1.817) in Fig. 3 hardly differ in spite of widely differing lattice configurations. However, comparing data for the first and second panels of Fig. 3, the lower occupancy in the latter requires its field-strength parameter k^2L^2 to be larger by the ratio 1.409 in order to maintain the phase advance of $80°$. This ratio becomes 1.616 for the third panel and reaches 5.941 for the low-occupancy case $\eta = 0.1$.

The exact results in Fig. 3 show, for a few examples, the insensitivity of peak beam excursion to changes in η and μ while σ_0 is held constant near the first-band midpoint. This insensitivity holds for wide-ranging values of η and μ, and can be predicted from Eq. (36) below. See Fig. 7 and Table I in App. D and the discussion of limiting cases in App. E.

Second passband:

Figure 4 shows a different situation in the second passband. The focus parameter θ has now been adjusted to give phase advance $\sigma_0 = 270°$ (the midpoint of the second band) in each case. Here, the peak radius varies considerably with the lattice parameters. The radii are 4.860, 7.386, and 6.742, respectively. The field-strength parameter $k^2L^2 = 2.25\,\pi^2$ required for the top panel must be increased by the factor 2.2985 when the occupancy is reduced by half and by the factor 2.5820 with occupancy 0.5 and asymmetry $\mu = 0.8$.

Note that the envelope minima in the focusing sections have very small values, which will be discussed in Sec. IX.

It is interesting that large envelope fluctuations in cases of large phase advance were found for a completely different case (solenoid focusing, zero emittance) by Lee and Briggs using both iterative analysis and simulation [9].

D. Close approximation for space charge effect

For the second and third panels in Fig. 3, we have chosen the same occupancies, drift asymmetries, and undepressed phase advances as those used in the simulations of Lund, Chilton, and Lee [10], Figs. 2b and 2c. Their
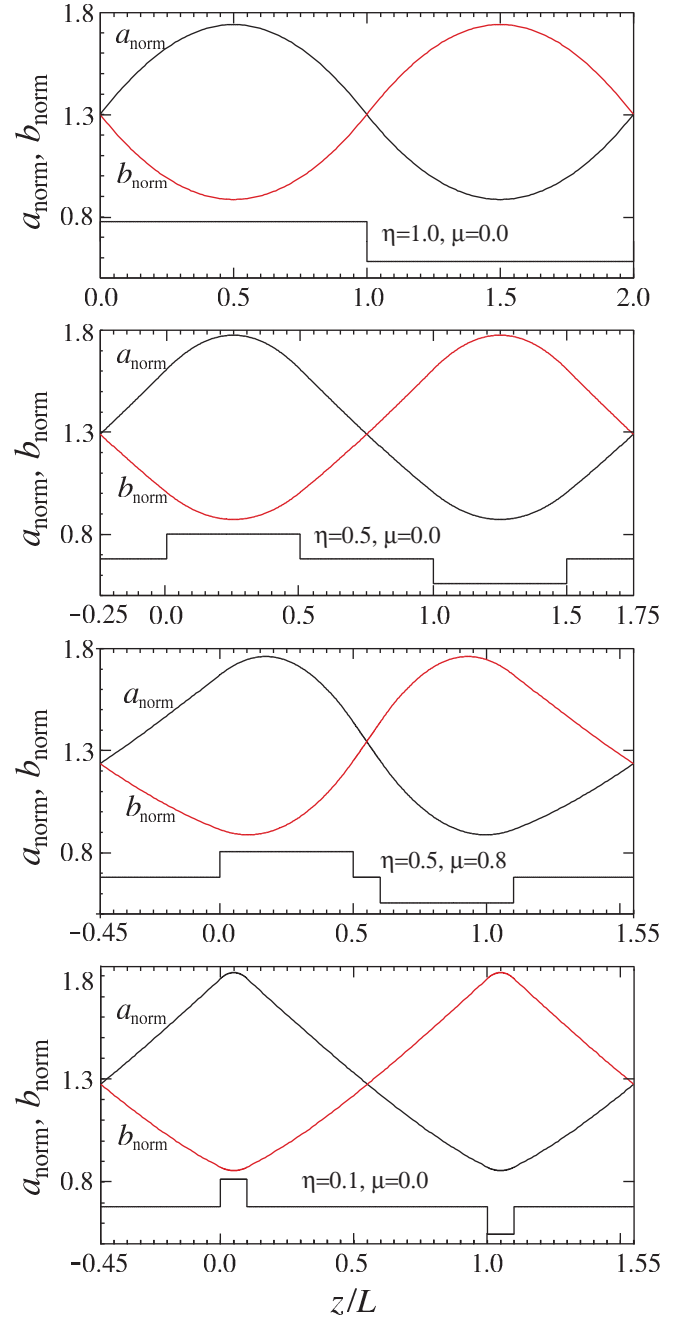

FIG. 3. Exact normalized envelope functions from Eqs. (31), (C8), (C9), and (C10). The normalized radii are defined by Eq. (33). Lattice parameters are as in Fig. 2. The value of kL for each panel is adjusted to give $\sigma_0 = 80°$, which is near the midpoint of each passband. The required values are $kL = 0.47642\pi$, 0.56546π, 0.60565π, and 1.16121π, respectively. The field strengths, which are proportional to k^2, thus change considerably while the peak envelopes remain nearly constant. See the contour plots and discussion in App. D. Note: These exact results are plotted conventionally, starting and ending at envelope crossover points. However, to agree with Fig. 1, $z = 0$ at start of focus section.

simulations used the charge parameter $Q = 4 \times 10^{-4}$, which depressed the phase advance from $80°$ to $24.74°$. Their envelope shapes appear very close to ours, indicating that their simulation results might be approximated by scaling our analytic results. Indeed, we find that the accuracy is of the order of 1%.

Scaling factor for space charge

To obtain a scaling factor for the case of the second panel of Fig. 3, we first note that its symmetries are the same as those assumed for the iterative analysis in Ref. [6]. We use formulae from Ref. [6] to calculate the beam envelope with and without space charge to about 0.5% accuracy. We take the ratio of the peak values to obtain the scaling factor and use that ratio to find the peak envelope with space charge for the case of the second panel. The result agrees with the simulation from
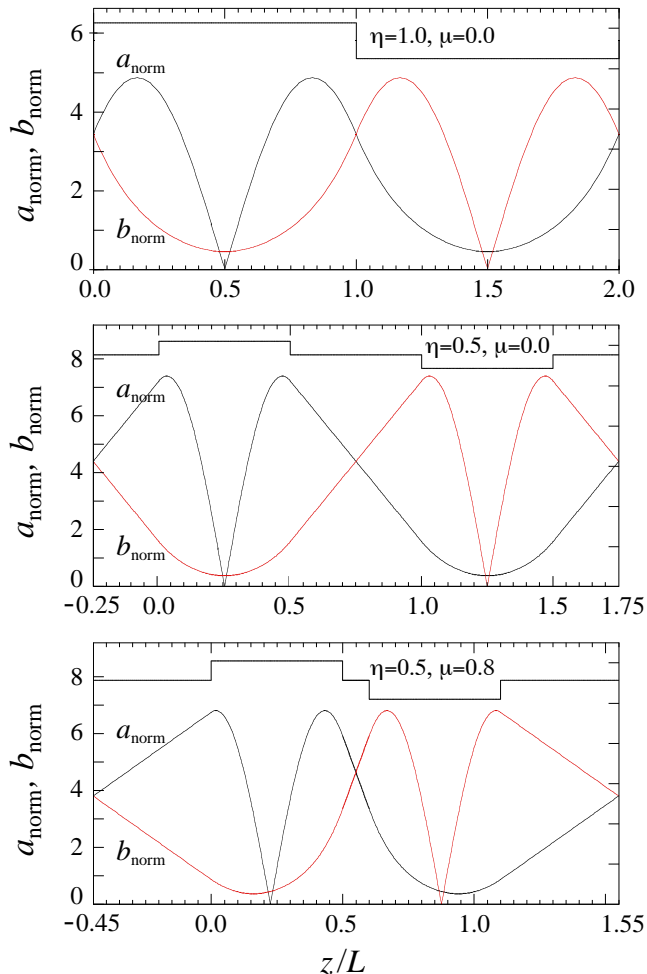

FIG. 4. Exact solutions of Eqs. (31), etc., with kL adjusted to give phase advance $\sigma_0 = 270°$, the midpoint of the narrow second passband seen in Fig. 2. Values of kL are 1.5π, 2.274106π, and 2.410273π, respectively. The effect of drift spaces on peak radius is larger here than for the first band (Fig. 3). See the contour plots and discussion in App. D.

Lund et al. [personal communication] to 1.1% accuracy. The same procedure gives the minimum envelope, the crossover envelope, and the crossover envelope angle to accuracies of -0.3%, 1.1%, and -0.2%, respectively.

Even though the formulae of Ref. [6] were derived for symmetric lattices, they can provide useful estimates even for cases of strong drift-length asymmetry, such as Fig. 3, third panel. The occupancy there is the same as in the second panel, and using the same scaling factors yields accuracies of 0.3%, 1.5%, 0.5%, and 3.6%.

With space charge, analytic solutions are apparently not available [5]. Iterative schemes, such as a conventional "shooting" method or the "IM" method of Ref. [10], have been employed. With some methods and for certain parameter regimes, it is difficult to find good starting seeds (initial guesses). In the case of shooting codes, the envelope radius and angle at the center of a drift space serve as suitable seeds. For these, our scaled results—although utilizing an unsyncopated model—give accuracies to within 0.5% and 3.6% for the strongly syncopated, strongly depressed case of Fig. 3, third panel. Using these seeds with the ESQPER code [11] gives convergence to 10^{-6} accuracy in about 20 iterations. Scaled solutions can also serve as the initial guess for iterative solutions of the "IM" type. Reference [10] describes various schemes iterating on numerically converged solutions to find solutions with given phase advance and emittances, current, or depressed phase advance. Our scaled results could be used to provide improved seeds for schemes with convergence difficulties, such as IM Case 0. See Sec. VB in Ref. [10].

VIII. PEAK ENVELOPE ANALYSIS

The peak envelope values (beam excursions) always occur in the focus segment. In the higher stable bands, minimum values occur there as well. For a given θ in the nth passband, we determine the locations z_m of the envelope extrema by differentiating Eq. (32) with respect to z and setting the result equal to zero. We find the roots

$$(1-2z_m/\eta L)\theta = \tan^{-1}\frac{\mu\nu\, sh}{B+sh} +$$
$$0,\ \pm\pi,\ \pm 2\pi,\ \pm\cdots,\ \pm(n-1)\pi, \quad (34)$$

where $m = 1,\cdots,2n-1$ and the principal value is used for $\tan^{-1}$. Note that the passband number is determined, given μ, η, and kL. One sees by inspection of Eq. (34) [or, indeed, of (32)] that the extrema are always spaced at equal z intervals $\Delta z_m/L = \pi/2kL$.

In the first passband focus segment, there is a single maximum; in the second, there is a minimum between two maxima, and so forth. Since, for any band n, all the maxima have equal value and since the first extremum is always a maximum, we need consider only the first of

the extrema. Then

$$z_1 = \frac{\eta L}{2}\left[1 - \frac{1}{\theta}\left(\tan^{-1}\frac{\mu\nu\,sh}{B+sh} + (n-1)\pi\right)\right] \qquad (35)$$

locates the maximum excursion of the envelope in the nth passband, and we get

$$a_{\max}^2(\theta) = \in\eta L\,\frac{F_{\max}^F}{\mathrm{P}\,\theta\,\sqrt{1 - (\frac{1}{2}\mathrm{Tr}\,\mathbf{M})^2}}, \qquad (36)$$

where

$$F_{\max}^F = F^F(z_1;\theta,\mu,\nu), \qquad (37)$$

with F^F given by Eq. (32).

Results for the first two passbands are plotted in Fig. 5. The lattice parameters are the same as for Figs. 2–4. Note the previous discussion of peak values in connection with those figures in Sec. VII C.

The minima of $a_{\max}$ with respect to kL (seen in Fig. 5) are plotted for the entire ranges of η and μ in App. D.
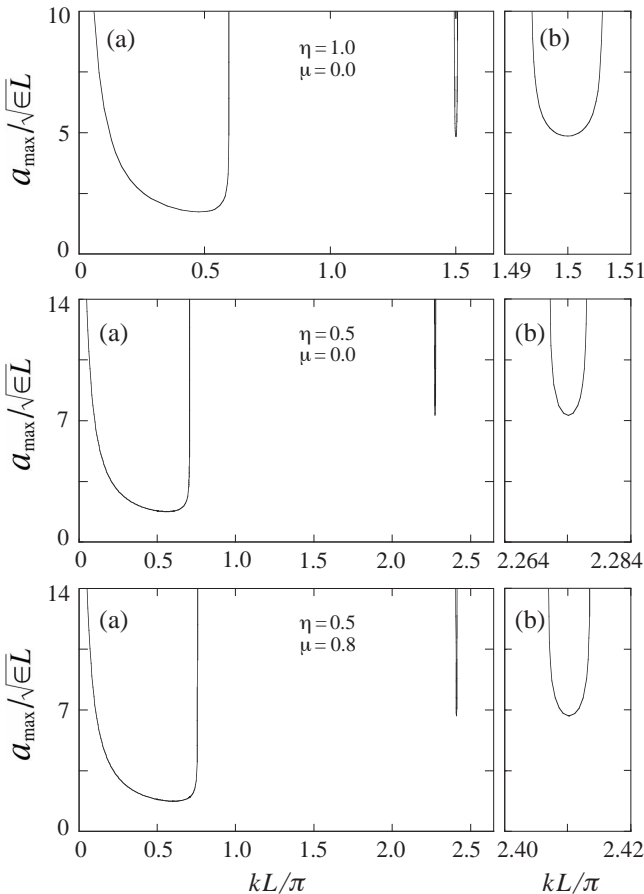

FIG. 5. Exact peak envelope functions, from Eq. (36), as functions of kL. Same lattice parameters (occupancy and asymmetry) as in Figs. 2, 3, and 4. (a) First two stable bands. (b) Second band magnified. Note the vertical scale change for the last two panels.

Limiting cases for $n = 1$ are analyzed in App. E, where the small variability of $a_{\max}$ with respect to η and μ in the vicinity of the first passband-midpoint is deduced from Eq. (36). Cases with $n > 1$ are analyzed in App. F.

IX. SECOND-BAND BEAM COMPRESSION

First we discuss the fully symmetric case ($\mu = 0$). Using differentiation of Eqs. (31) and (C9) or symmetry arguments, it is easy to see that for the even passbands, $a(z)$ has a minimum at the center of the focus section and again a minimum at the center of the defocus section. The same is true for $b(z)$ [Eq. (3)], so that the beam area $A(z) = \pi\,a(z)b(z)$ can become very small at those points. (See Fig. 4.) We define the compression ratio

$$R \equiv \frac{\max(A)}{\min(A)}.$$

In general, to calculate the beam area in the focus segment, we first find $a(z)$ from Eq. (31) and then $b(z)$ from Eq. (3). The latter requires $a(z)$ in the defocus segment, i.e., Eqs. (C9).

The maximum beam area occurs at the midpoint of the narrower of the drift spaces. It is found from Eqs. (C8) or Eqs. (C10).

Figure 4 shows exact beam envelopes for the midpoint of the second passband. In the first panel, the ratio R of maximum to minimum beam areas is 0.59×10^3. In the second panel, with η reduced from 1.0 to 0.5, R increases to 2.68×10^3. In the third panel, with large drift-length asymmetry ($\mu = 0.8$), R is 2.44×10^3, only slightly less than for the second panel. The value of the first a minimum depends strongly on η and weakly on μ. Additional results and discussion are presented in App. D (see Fig. 9).

Previously, Ref. [3] showed that, for the FD model, the compression effect is greatly augmented for phase advances near a passband edge (Fig. 9)—and noted that caveats apply. Then, Ref. [7] treated the FoDO case. It compared compressions at half occupancy near the band edge for symmetric and asymmetric drift spaces. The phase advances σ_0 were $356.75°$ and $356.6°$, respectively. A large change in R was noted. Here, we present the same comparison, holding both phase advances to $356.58°$. For the symmetric case ($\mu = 0.0$), the nominal compression ratio $R = 1.06 \times 10^6$ is large because the first b minimum is very small. In the second case, drift asymmetry ($\mu = 0.8$) shifts the minimum of $a(z)$ away from this point and reduces R to 6.93×10^4 (see Fig. 6).

Space charge would also affect the beam compression. The effect on the beam waist could be small because emittance pressure scales more rapidly with radius than does space-charge pressure.

We note again that the strong focusing fields needed for the second passband violate the KV paraxial model. The WARP particle code [12] could determine how severe the effect is.
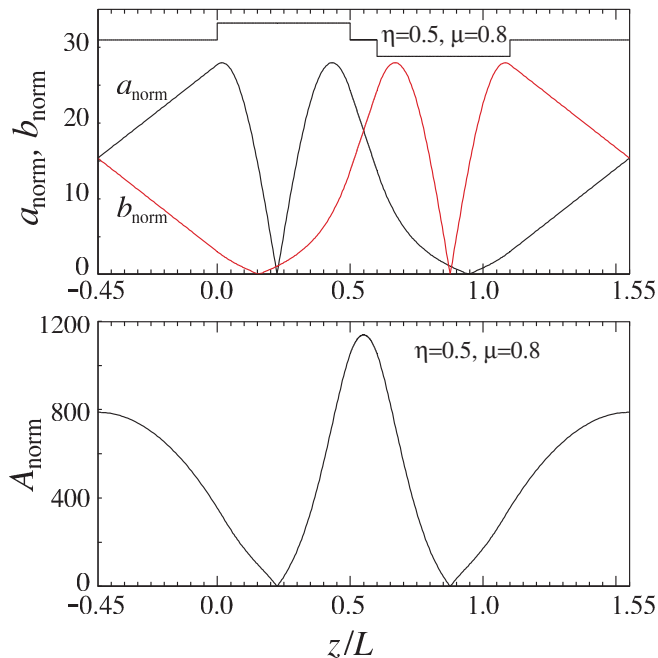
FIG. 6. Envelope functions $a_{\mathrm{norm}}(z)$, $b_{\mathrm{norm}}(z)$, and beam area $A_{\mathrm{norm}}(z) \equiv \pi a_{\mathrm{norm}} b_{\mathrm{norm}}$ near the outer edge of the second passband. For this case, $kL = 2.41361\pi$, giving $\sigma_0 = 356.58°$ (cf. third panel of Fig. 4). The drift asymmetry ($\mu = 0.8$) causes the a and b minima to separate (top panel), reducing the beam compression (see text).

X. DISCUSSION

We have obtained exact matched-beam envelopes for the FoDO lattice model, which specifies focus occupancy η and drift-space asymmetry μ. From these solutions we have derived an exact equation for the peak envelope excursion as a function of η, μ, and the field-strength parameter $k^2 L^2$.

First passband

Our primary finding for the first passband is the remarkable insensitivity of the peak envelope excursion to variations of the lattice parameters η and μ over their entire ranges. We find that the corresponding values of kL depend weakly on μ and increase by about 30% as η decreases from unity to 0.5 (see App. D). Thus, the present paper shows that the practical necessity of occupancies η smaller than one does not drastically increase kL.

Second passband

We begin our discussion of the second passband by recalling our earlier study of the FD model [3], where we showed why the second band is impractical for beam transport and how it could be useful for novel applications. We found that the field strength required for minimum beam size is about an order of magnitude larger than for the first passband and that the beam excursions swell by a factor ~ 2.5. Furthermore, the width of the second passband is so narrow that it would take great effort to set and maintain the correct field strength. The strong fields would be difficult to apply and would likely violate the paraxial assumption of the KV equations.

For the FoDO case, the present paper shows that the required field strength again depends only weakly on μ. The dependence on η, however, is stronger in the second band: the kL required for minimum beam size with $\eta = 0.5$ exceeds that for $\eta = 1$ by about 70% (see App. D). The above practical problems of the second passband are, then, exacerbated. Nevertheless, we have presented second-band quantitative results here in some detail, because although the existence of higher passbands is well known and they have attracted some interest (see, e.g., Ref. [13]), we have not found their solutions explored elsewhere.

We have also analyzed the second passband to investigate the possibility of applications beyond ordinary beam transport. Such applications could take advantage of the small envelope minima in both focusing planes at certain z locations (for even bands).

Note that these minima, though small, are unequal in size. For the case $\eta = 0.5$, $\mu = 0$, the beam has an elliptical waist with axis ratios ranging from 20.07 at $\sigma_0 = 270°$ to 14.33 at $\sigma_0 = 346.6°$. In this range the compression ratio rises from 2.7×10^3 to 69.4×10^3 but at the expense of doubling the already large peak envelope amplitude. Therefore, any attempt to observe or utilize the second passband in practice should try to operate at the passband center.

Conceivably, one could utilize the periodicity of the double beam-waists to provide powerful differential pumping of the beam line using a series of small elliptical apertures. Another possibility is the direct production of an external beam with small spot size at the end of a quadrupole-focused accelerator. Much research would be needed first to resolve the practical issues observed in Ref. [3].

Our exact results throughout this paper apply to the zero-space-charge limit. For cases where space charge dominates, Sec. VII D describes, for the first passband, a method for finding good approximations for beam-envelope amplitudes and angles. (Note that it utilizes the formulae of Ref. [6], which were developed only for the first passband.) This method could be useful for surveying large regions of parameter space and finding initial values for simulations.

Appendix A: PHASE-AMPLITUDE METHOD

In their 1958 paper [1], Courant and Snyder described the phase-amplitude method for dealing with equations having the form of Eq. (13) [or (A1)] and applied it to obtain an approximate solution to the alternating-gradient problem. Their paper introduced a number of powerful concepts — beta function, Courant-Snyder invariant, etc.—which have been used by many authors, in various ways, to derive the envelope function for a given focusing function. The Courant-Snyder concepts are not needed for our present work. We use a somewhat simplified treatment to derive the solution [Eq. (B4)] in this appendix and the next one. These make this paper fairly self-contained and, we hope, accessible to the non-specialist. One may also refer to standard textbooks, such as Wiedemann's [14].

Without space charge, the transverse position $x(z)$ of a single particle obeys the linear equation

$$x''(z) + f(z)x(z) = 0. \tag{A1}$$

(We assume here that $f(z)$ is a periodic function.) One can verify by substitution that

$$x = \frac{a(z)}{\sqrt{\in}}(C_1 \cos\psi + C_2 \sin\psi) \tag{A2}$$

is the general solution of Eq. (A1), provided that $a(z)$ satisfies Eq. (12) and that

$$\psi' = \frac{\in}{a^2}. \tag{A3}$$

The quantities $\psi(z)$ and $a(z)$ are known as the phase and amplitude. If we differentiate Eq. (A2) and use Eq. (A3), we get

$$\sqrt{\in}x' = (C_1 a' + C_2 \in/a)\cos\psi + (C_2 a' - C_1 \in/a)\sin\psi. \tag{A4}$$

Set $\psi(z_0) = 0$. Then

$$C_1 = \sqrt{\in}\, x_0/a_0; \tag{A5}$$

$$C_2 = (a_0 x_0' - a_0' x_0)/\sqrt{\in}. \tag{A6}$$

Inserting these into Eq. (A2) gives

$$x(z) = g_{11}(z, z_0)\, x_0 + g_{12}(z, z_0)\, x_0'; \tag{A7a}$$

$$x'(z) = g_{21}(z, z_0)\, x_0 + g_{22}(z, z_0)\, x_0'. \tag{A7b}$$

where the coefficients g_{ij} can be deduced from Eqs. (A2), (A4), (A5), and (A6). In App. B we will need the coefficient g_{12}, which is

$$g_{12}(z, z_0) = \frac{1}{\in}a_0 a(z)\sin\psi. \tag{A8}$$

At this point, we specify that the beam is matched, i.e., $a(z)$ is periodic with the same period, $2L$, as the lattice. Then $a(z_0 + 2L) = a(z_0)$. We define

$$\psi(z_0 + 2L) \equiv \sigma_0, \tag{A9}$$

the phase advance for a whole period, and observe from Eq. (A3) that, for the matched beam, σ_0 is independent of the choice of z_0. Then, writing Eqs. (A7) in matrix form for the case $z = z_0 + 2L$, we have

$$\begin{pmatrix} x(z+2L) \\ x'(z+2L) \end{pmatrix} = \begin{pmatrix} g_{11}(z+2L, z) & \frac{1}{\in}a^2(z)\sin\sigma_0 \\ g_{21}(z+2L, z) & g_{22}(z+2L, z) \end{pmatrix} \begin{pmatrix} x(z) \\ x'(z) \end{pmatrix}. \tag{A10}$$

We drop the subscript on z_0 because the location of z_0 is arbitrary. Note that the matrix elements here are periodic but $x(z)$ is not. If one writes out g_{11} and g_{22}, one sees that the trace has the value

$$g_{11} + g_{22} = 2\cos\sigma_0, \tag{A11}$$

which is independent of z.

Appendix B: MATCHED ENVELOPE SOLUTION

Now we calculate the matched beam envelope for a machine with periodic focusing function $f(z)$. In general, there is a machine matrix $\mathbf{M}(z)$, obtainable in principle by integrating Eq. (A1). (Analytic results are easily obtainable if $f(z)$ is piece-wise constant, but not in most other cases.) The result gives the phase-space change over a whole machine period (for the specific FoDO example, see Secs. V and VII A):

$$\begin{pmatrix} x(z+2L) \\ x'(z+2L) \end{pmatrix} = \begin{pmatrix} M_{11}(z) & M_{12}(z) \\ M_{21}(z) & M_{22}(z) \end{pmatrix} \begin{pmatrix} x(z) \\ x'(z) \end{pmatrix}. \tag{B1}$$

Comparing Eqs. (B1) and (A10) and using Eq. (A11) shows that

$$2\cos\sigma_0 = M_{11} + M_{22} = \mathrm{Tr}\,\mathbf{M} \tag{B2}$$

and

$$M_{12} = \frac{1}{\in}a^2(z)\sin\sigma_0 \tag{B3}$$

or

$$\frac{1}{\in}a^2(z) = \frac{M_{12}(z)}{P\sqrt{1 - (\frac{1}{2}\mathrm{Tr}\,\mathbf{M})^2}}, \tag{B4}$$

where

$$P(\sigma_0) \equiv \mathrm{sign}(\sin\sigma_0) \tag{B5}$$

gives the correct branch of the radical and ensures that the right-hand side of Eq. (B4) is always positive.

Various versions of Eq. (B4) have appeared in the literature — for example, Eq. (19) in Ref. [10].

The criterion for single-particle stability [Eq. (20), Sec. V] is $|\mathrm{Tr}\,\mathbf{M}| < 2$. Notice from Eq. (B4) that the

criterion for existence of a real solution for the envelope equation is the same. Therefore, existence implies stability and vice versa.

In the stable regions, specializing to FoDO, Eq. (B5) is equivalent to

$$P(\theta) \equiv \text{sign}(\sin \theta). \tag{B6}$$

Equation (B6), which was noted in Ref. [3], follows easily from Eq. (24) if $\eta = 1$. A brief calculation shows that Eq. (B6) applies without modification for general η and μ.

Appendix C: EXACT ENVELOPES IN THE DRIFT AND DEFOCUS SEGMENTS

In the main text, we gave details of the envelope calculation for the focus segment. Here, we briefly describe our method for the three remaining segments and give the results.

The envelope calculation for any segment is simplified by moving the origin to the beginning of the segment. Thus, the matrices that will yield the envelopes for the three remaining segments are

$$\mathbf{M}^{O_1}(z) = \begin{pmatrix} 1 & z \\ 0 & 1 \end{pmatrix} \mathbf{M}_F \, \mathbf{M}_{O_2} \mathbf{M}_D \begin{pmatrix} 1 & d_1 - z \\ 0 & 1 \end{pmatrix}, \tag{C1}$$

$$\mathbf{M}^D(z) = \begin{pmatrix} \cosh kz & \frac{1}{k}\sinh kz \\ k\sinh kz & \cosh kz \end{pmatrix} \mathbf{M}_{O_1}\mathbf{M}_F \, \mathbf{M}_{O_2} \times$$
$$\begin{pmatrix} \cosh k(\eta L - z) & \frac{1}{k}\sinh k(\eta L - z) \\ k\sinh k(\eta L - z) & \cosh k(\eta L - z) \end{pmatrix}, \tag{C2}$$

$$\mathbf{M}^{O_2}(z) = \begin{pmatrix} 1 & z \\ 0 & 1 \end{pmatrix} \mathbf{M}_D \, \mathbf{M}_{O_1}\mathbf{M}_F \begin{pmatrix} 1 & d_2 - z \\ 0 & 1 \end{pmatrix}. \tag{C3}$$

Note that the cyclic order is maintained in all cases.

After performing the matrix multiplications, one obtains envelopes from Eq. (B4), using $\mathrm{M}_{12}^{O_1}, \mathrm{M}_{12}^{D}$, and $\mathrm{M}_{12}^{O_2}$.

First, as in Sec. VII A, we define dimensionless quantities

$$F^{O_1} \equiv k\,\mathrm{M}_{12}^{O_1}, \tag{C4}$$

$$F^{D} \equiv k\,\mathrm{M}_{12}^{D}, \tag{C5}$$

$$F^{O_2} \equiv k\,\mathrm{M}_{12}^{O_2}. \tag{C6}$$

We write Eq. (31) as

$$a^2(z) = \in \eta L \, \frac{F^j(z)}{\mathrm{P}\,\theta\,\sqrt{1 - (\frac{1}{2}\mathrm{Tr}\,\mathbf{M})^2}}, \tag{C7}$$

where the superscript j represents F, O_1, D, or O_2.

For the first drift segment, the exact envelope is obtained from Eq. (C7) and

$$F^{O_1} = G_1 - 2\,H_1\,k\,z + J_1\,k^2 z^2, \tag{C8a}$$

where

$$G_1 \equiv 2\,\nu\,ch\,cs + \nu_1\,sh\,sn + ch\,sn + (1 + 2\,D)\,sh\,cs; \tag{C8b}$$

$$H_1 \equiv (1 + D)\,sh\,sn + \nu\,ch\,sn + \mu\,\nu\,sh\,cs; \tag{C8c}$$

$$J_1 \equiv \nu_2\,sh\,sn + ch\,sn - sh\,cs; \tag{C8d}$$

$$D \equiv 0.5\,(1 - \mu^2)\,\nu^2. \tag{C8e}$$

For the defocus segment,

$$F^D = E_d\,sh + B_d\,ch + \mu\,\nu\,sn\,\sinh\zeta + (sn + B_d)\cosh\zeta, \tag{C9a}$$

where

$$B_d \equiv \nu\,cs - D\,sn; \tag{C9b}$$

$$E_d \equiv cs - \nu\,sn; \tag{C9c}$$

$$\zeta \equiv \theta(1 - 2z/\eta L). \tag{C9d}$$

For the second drift segment,

$$F^{O_2} = G_2 + 2\,H_2\,k\,z + J_2\,k^2 z^2, \tag{C10a}$$

where

$$G_2 \equiv 2\,\nu\,ch\,cs - \nu_2\,sh\,sn + (1 - 2\,D)\,ch\,sn + sh\,cs; \tag{C10b}$$

$$H_2 \equiv (1 - D)\,sh\,sn - \mu\,\nu\,ch\,sn + \nu\,sh\,cs; \tag{C10c}$$

$$J_2 \equiv \nu_1\,sh\,sn + ch\,sn - sh\,cs. \tag{C10d}$$

These exact results, together with those from Sec. VII A, were used to plot the solutions shown in the main text.

Appendix D: RESULTS OF PARAMETER STUDIES

We have explored the dependence of our solutions on the FoDO lattice parameters η and μ and the focus parameter k (or, alternatively, σ_0). Key results were presented in Sections V, VII C, VIII, and IX. In this Appendix, we present additional details of the parameter studies.

The peak envelope excursion, $a_{\max}$, for the first passband was discussed in Sec. VII C, where its insensitivity to η and μ at fixed σ_0 was shown for a few representative cases. Then, Section VIII expressed $a_{\max}$ as a function of θ and Fig. 5 showed the broad minimum of $a_{\max}$ with varying focus strength. We found that for full occupancy ($\eta = 1$), the peak radius remains near its minimum as the focus parameter θ ranges from 0.446π to 0.506π, yielding phase advances σ_0 in the range $69° - 93°$. The peak radius in this range is constant to within $\pm 0.5\%$. For $\eta = 0.5$, the σ_0 range is $62°$ to $96°$.

In Fig. 7 we present results, in the form of contour plots, of a survey over the entire range of η and μ for the first and second passbands. We examine $a_{\max}^{\min}$, defined to be $a_{\max}(\theta)$ [Eq. (36)], minimized with respect to θ.

[Fig. 5 (a_{max} vs. θ) had shown these minimum values for just three combinations of η and μ.]

In the first passband (upper panel of Fig. 7), a_{max}^{min} exhibits non-trivial structure, approaching a saddle point at $\eta = .6$, $\mu = 1$; but the numerical value of a_{max}^{min} changes very little over the entire range of η and μ (see the contour levels in Table I). The second passband (lower panel), on the other hand, shows a weak variation of a_{max}^{min} with respect to drift asymmetry (except at very small occupancy); but a strong variation with occupancy, diverging as $\eta \to 0$; it lacks the saddle point but is ill behaved at $\eta = 1$, $\mu = 1$.

The focusing-field strength—proportional to $k^2 L^2$—is a critical parameter in machine design. In Fig. 8, we plot the kL required for minimum peak-envelope amplitude
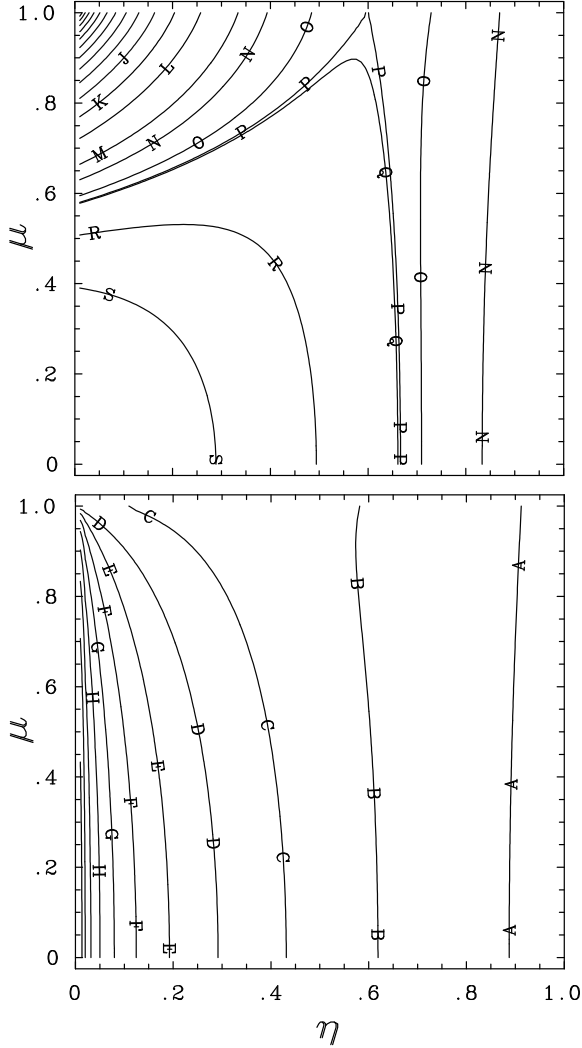

FIG. 8. Contour plots of kL at which $a_{max} = a_{max}^{min}$ (see Fig. 7), as a function of η and μ for the first passband (upper panel) and second passband (lower panel).

FIG. 7. Contour plots of $a_{max}^{min}/\sqrt{\in L}$ as a function of η and μ. The contour levels are given in Table I, which shows a weak variation for the first passband (upper panel) and a strong variation for the second passband (lower panel).
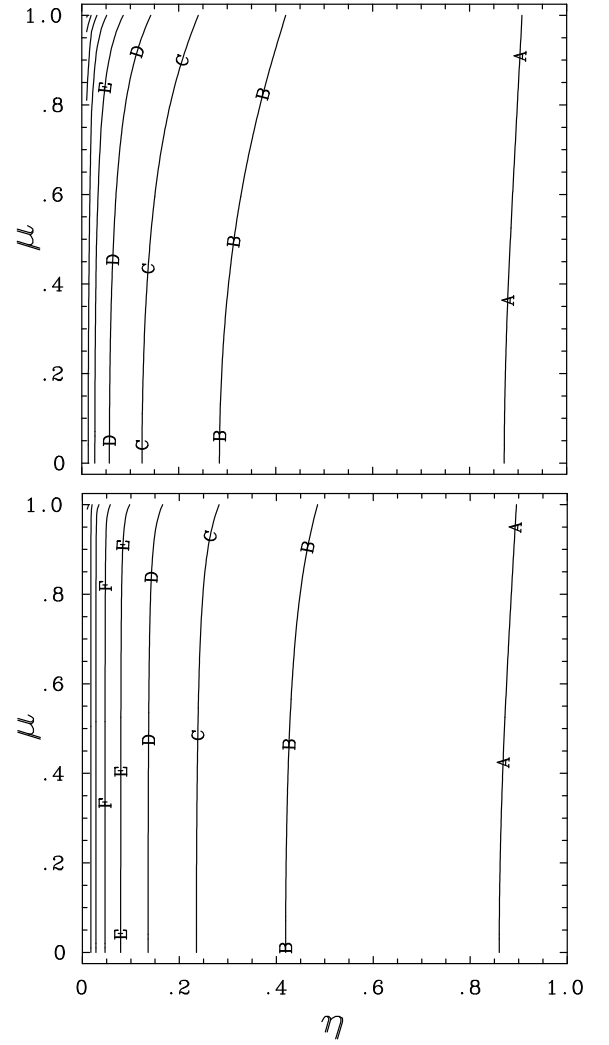
TABLE I. Table showing values of contours in Figs. 7–9

Fig. 7a		Fig. 7b		Fig. 8a		Fig. 8b		Fig. 9	
I	1.6571	A	5.056	A	1.516	A	4.898	A	6.838E+2
J	1.6764	B	6.407	B	2.215	B	8.307	B	2.374E+3
K	1.6958	C	8.118	C	3.235	C	14.09	C	8.244E+3
L	1.7156	D	10.29	D	4.726	D	23.89	D	2.862E+4
M	1.7355	E	13.04	E	6.902	E	40.51	E	9.939E+4
N	1.7460	F	16.52	F	10.08	F	68.70	F	3.451E+5
O	1.7557	G	20.93	G	14.73	G	116.5	G	1.198E+6
P	1.7595	H	26.52	H	21.51	H	197.5	H	4.160E+6
Q	1.7600	I	33.61	I	31.42	I	335.0	I	1.445E+7
R	1.7761	J	42.59					J	5.016E+7
S	1.7967	K	53.96					K	1.742E+8

at given η and μ; i.e., we plot kL at the minimizing θ found for Fig. 7. For both passbands, the dependence on μ is weak; kL increases as the occupancy decreases and
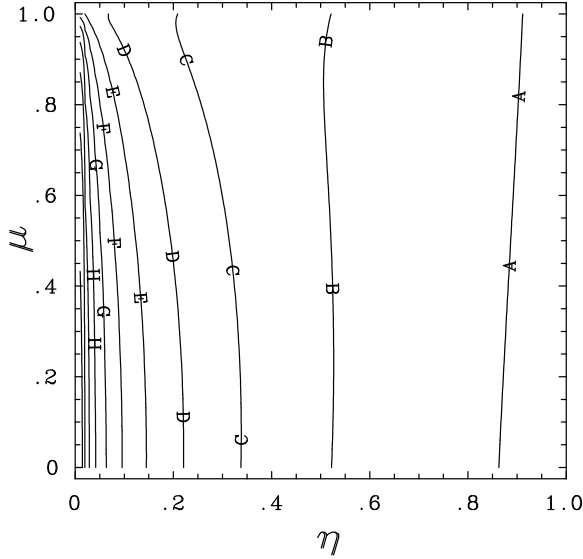
FIG. 9. Contour plot of the beam compression ratio for peak-minimizing values of kL in the second passband. Note the very strong compression at small occupancies (see Table I).

diverges as the occupancy goes to zero. For the second passband, however, the dependence on η is stronger (see the contour-levels in Table I).

Finally, in Fig. 9 we plot the compression ratio R for the second passband. At each (η, μ) point, kL is the same as for the lower panel of the previous two figures. The dependence on drift asymmetry is again weak compared to the dependence on occupancy, except at very small occupancy. Note the very rapid increase in compression as the occupancy is reduced (Table I). Although the compression-ratio contours are very similar to the $a_{\max}^{\min}$ contours, their values in the table rise much more steeply with reduced η, showing that the major effect on R arises from reduced beam-waist size.

Appendix E: LIMITING CASES — FIRST PASSBAND

Appreciable insight into Figs. 7 and 8 can be gained from an examination of limiting cases.

We look first at θ_n [Eq. (27)], having observed from our numerical results that the minimizing θ is very near θ_n. For $n > 1$, this is obvious, given the denominator in Eq. (31) and the narrowness in θ of the higher stable bands. For the first passband, it is also true: Our results show that $(\theta_n - \theta)/\theta_n$ is insensitive to μ; it is about 0.04 at $\eta = 1$; and it increases slowly as η decreases, to ~ 0.075 at $\eta = 0.05$. (Our contour plot, Fig. 8, shows kL, not θ, but the θ behavior is easily inferred, since $\theta \equiv \eta kL$.)

In the following, we refer to regions I, II, and III. Roughly, these occupy the right, central, and left portions of Fig. 7.

From Eq. (27), we see that $n = 1$ is a special case: only $n = 1$ can have a solution at small θ_n. On the other hand,

θ_1 can never be large. Nor, again from Eq. (27), when $\theta_1 \sim \mathcal{O}(1)$ can ν be very large. So we choose the following expansions:

$$\frac{\theta_1}{\pi/2} \xrightarrow[(\nu \ll 1)]{}$$
$$\text{I}: \quad 1 - \frac{1-\eta}{\eta} + \left(\frac{1-\eta}{\eta}\right)^2 \left[1 + \frac{\pi}{2} \tanh\left(\frac{\pi}{2}\right) \frac{1+\mu^2}{2}\right]$$

and

$$\theta_1 \xrightarrow[(\theta_1 \ll 1)]{} \left[\frac{\eta/(1-\eta)}{\frac{2}{3} + \frac{1-\mu^2}{2}\frac{1-\eta}{\eta}}\right]^{1/4} \rightarrow$$

$$\begin{cases} \text{II}: \quad \left(\frac{3}{2}\frac{\eta}{1-\eta}\right)^{\frac{1}{4}}, & \theta_1 \ll 1, \ \frac{1-\mu^2}{2}\frac{1-\eta}{\eta} \ll \frac{2}{3}; \\ \text{III}: \quad \left(\frac{\eta}{1-\eta}\right)^{\frac{1}{2}}\left(\frac{2}{1-\mu^2}\right)^{\frac{1}{4}}, & \theta_1 \ll 1, \ \frac{1-\mu^2}{2}\frac{1-\eta}{\eta} \gg \frac{2}{3}. \end{cases}$$

In each region, we have calculated only through the terms needed to obtain the lowest-order variations of $a_{\max}^{\min}$ below. Note the weak dependence on parameters: weaker upon μ than η in region I; and weak in regions II and, except at very small η, III. The only strong variation occurs as $\eta \to 0$, when $\theta_1 \propto \sqrt{\eta} \to 0$. Note also that θ_1 spans the full range where $\tan\theta$ in Eq. (27) is positive in the first passband, from $\theta_1 = 0$, at $\eta = 0$, to $\pi/2$ at $\eta = 1$.

The boundary between regions II and III $\left(\frac{1-\mu^2}{2}\frac{1-\eta}{\eta} = \frac{2}{3}\right)$ is a line that extends from $\mu = 1$, $\eta = 0$ to $\mu = 0$, $\eta = 3/7$. $\theta_1 = 1$ restricts region II to the left of $\eta = 0.4$. (The general small-θ_1 expansion is valid at slightly larger η for small μ.) Region I extends from $\eta = 1/2$ [where $(1-\eta)/\eta = 1$] to $\eta = 1$. Note that there is a region at intermediate η, between regions I and II, where θ_1 and ν are $\mathcal{O}(1)$ and none of the above expansions is valid. One could of course expand around some intermediate η; but since the variations for intermediate η remain weak and we are concerned here only with finding the major trends, we do not carry that out.

Next, we evaluate $a_{\max}^2$ [Eq. (36)] at $\theta = \theta_1$, in the same limits as above, to obtain an approximate $a_{\max}^{\min}$. We find:

$$\frac{a_{\max}^{\min\,2}}{\in L} \sim \begin{cases} \text{I}: \quad \frac{\cosh\frac{\pi}{2} + \sinh\frac{\pi}{2}}{\pi/2}\left[1 + \frac{(1-\eta)^2}{\eta}(1+\mu^2)\times \right. \\ \qquad \left. (\frac{\pi}{2}-1)\frac{\pi}{4}\tanh(\frac{\pi}{2})\right]; \\ \text{II}: \quad 2 + \frac{3}{2}\frac{(1-\eta)^{3/2}}{\eta^{1/2}}(1-\mu^2) \\ \text{III}: \quad 2 + (1-\eta)\left[2(1-\mu^2)\right]^{1/2} \end{cases}$$

At $\eta = 1$, this gives $a_{\max}^{\min}/(\in L) \sim 1.75$, which agrees well with Table I. $a_{\max}^{\min}$ decreases with η and increases with μ as $\eta \to 1$; but the variation is very weak, appearing only at second order in $1-\eta$ (the first-order terms cancelled). In regions II and III, the variations with parameters are again weak (see the expansion parameters given for θ_1). In region II, $a_{\max}^{\min}$ decreases with η, more weakly as η and μ increase; and $a_{\max}^{\min}$ decreases with μ, more weakly as $\eta \to 1$. In region III, $a_{\max}^{\min}$ decreases with η, more weakly as η and $\mu \to 1$; and $a_{\max}^{\min}$ decreases with μ, more

weakly as η increases and μ decreases. Thus the trends and structure observed in Fig. 7—the insensitivity in the first passband of $a_{\max}^{\min}$ to parameters and the presence of the saddle point—are found within this simple analysis.

Appendix F: LIMITING CASES — HIGHER PASSBANDS

We mentioned earlier that, for $n > 1$, the minimizing θ is obviously very near θ_n because of the narrowness in θ of the higher stable bands. We note from Sec. VI and Eq. (27) that $(n-1)\pi < \theta_n < (n-\frac{1}{2})\pi$. Here, then, we expand Eq. (27) to lowest order around large θ_n, so that $\tanh\theta_n \to 1$. We find to first order in the remaining small parameters:

$$\theta_n = \begin{cases} \text{I}: & (n-\tfrac{1}{2})\pi - \nu_n, & \nu \ll 1; \\ \text{II}: & (n-\tfrac{3}{4})\pi + \frac{1}{2\nu_n} - \frac{1-\mu^2}{2}\frac{\nu_n}{2}, & \nu \gg 1,\ \frac{1-\mu^2}{2}\nu \ll 1; \\ \text{III}: & (n-1)\pi + \frac{2}{1-\mu^2}\frac{1}{\nu_n}, & \nu \gg 1,\ \frac{1-\mu^2}{2}\nu \gg 1. \end{cases}$$

Again, regions I, II, and III refer, roughly, to the right, central, and left portions of Fig. 7.

ν_n stands for ν with θ evaluated at the lowest-order θ_n, i.e., at the leading term in each of the three cases above. For $n = 2$, the border between cases I and II ($\nu_n = 1$) occurs at $\eta \sim 0.8$. The border between cases II and III ($1 - \mu^2 = 2\nu_n$) runs from $\mu = 1$, $\eta = 0$ to $\mu = 0$, $\eta \sim 0.64$. For case II, note also that the two first-order terms cancel on a line above and to the right of the II/III border, inter-

cepting $\mu = 0$ at $\eta \sim 0.74$. The limiting cases thus cover the entire space (although of course more terms would be needed for accurate expressions near the expansion limits).

From these results we see that θ_n spans its full possible range, going from $(n-1)\pi$ at $\eta = 0$ to $(n-\frac{1}{2})\pi$ at $\eta = 1$. To lowest order, θ_n is constant in each of the three regions; the first-order terms vary with parameters in a direction to make θ_n approach the neighboring region's constant. For the second passband, there is only a 50% variation in θ_n over the entire range of η and μ. The μ-dependence is weak: it enters only at first order, and only for cases II and III, and is appreciable there only for μ near unity. Fig. 8 together with Table I confirms these results. At the minimizing θ, then, $kL \sim (n-\frac{3}{4})\pi/\eta$—the focus-parameter strength varies approximately inversely with the occupancy.

For $a_{\max}^2$ at $\theta = \theta_n$, we find to lowest order:

$$\frac{a_{\max\,n}^{\min\,2}}{\in L} \sim \begin{cases} \text{I}: & \frac{e^{(n-\frac{1}{2})\pi}}{(n-\frac{1}{2})\pi}; \\ \text{II}: & \frac{e^{(n-\frac{3}{4})\pi}}{(n-\frac{3}{4})\pi}\frac{\eta\nu}{2}\left(\sqrt{2} + \sqrt{1+\mu^2}\right); \\ \text{III}: & \frac{e^{(n-1)\pi}}{(n-1)\pi}\frac{\eta(1-\mu^2)}{4}\nu^3. \end{cases}$$

Note that the μ-dependence is again weak, but the trends are opposite for cases II and III, as born out by the lower panel of Fig. 7; and that, from case III, $a_{\max}^{\min} \propto 1/\eta$ as $\eta \to 0$.

[1] E. D. Courant and H. S. Snyder, Ann. of Phys. **3**, 1 (1958).

[2] O. A. Anderson and L. L. LoDestro, in *Proc. 2007 Particle Accelerator Conference, Albuquerque, NM* (IEEE, 2007).

[3] O. A. Anderson and L. L. LoDestro, Phys. Rev. ST Accel. Beams **12**, 054201 (2009).

[4] I. M. Kapchinskij and V. V. Vladimirskij, in *Conf. on High Energy Accel. and Instrum.* (CERN Sci. Inf. Service, Geneva, 1959) p. 274.

[5] S. M. Lund and B. Bukh, Phys. Rev. ST Accel. Beams **7**, 024801 (2004).

[6] O. A. Anderson, Phys. Rev. ST Accel. Beams **10**, 034202 (2007).

[7] O. A. Anderson and L. L. LoDestro, in *Proc. 2009 Particle Accelerator Conference, Vancouver, BC* (IEEE, 2009).

[8] M. Reiser, Particle Accelerators **8**, 167 (1978).

[9] E. P. Lee and R. J. Briggs, Tech. Rep. LBNL-40774, UC 419 (Lawrence Berkeley National Laboratory, 1997).

[10] S. M. Lund, S. H. Chilton, and E. P. Lee, Phys. Rev. ST Accel. Beams **9**, 064201 (2006).

[11] The ESQPER code is based on the ESQACL code, with the addition of an iterative loop. The reference for ESQACL is: L. Soroka and O.A. Anderson, in *Proc. Computational Accelerator Physics Conference (CAP93), Pleasanton, CA* (AIP, 1993).

[12] D. P. Grote, A. Friedman, I. Haber, W. Fawley, and J.-L. Vay, Nucl. Instrum. and Meth. **A 415**, 428 (1998).

[13] R. Pakter and F. B. Rizzato, Phys. Rev. E **65**, 056503 (2002).

[14] H. Wiedemann, *Particle Accelerator Physics* (Springer-Verlag, New York, 1993).